Effect of lithium concentration on the thermal and optical properties of $Li_xMn_2O_4$ by photoacoustic measurements

S. Thomas Lee,[1] K. Raveendranath,[2] M. Rajive Tomy,[2] M. Paulraj,[1] S. Jayalekshmi,[2] K. P. R. Nair,[2] and Jyotsna Ravi[1]
[1]*Departamento de Fisica, Universidad de Concepcion, Casilla 160-C, Concepcion, Chile*
[2]*Department of Physics, Cochin University of Science and Technology, Cochin-682022, India*
(Received 25 January 2007; revised manuscript received 12 June 2007; published 13 September 2007)

In the present work, pellets of $Li_xMn_2O_4$ polycrystalline powder samples with $x=0.8$, 0.9, 1.0, 1.1, and 1.2 are analyzed to understand the effect of lithium concentration on the thermal and optical properties, and the electronic structure of $Li_xMn_2O_4$ predicted in an earlier work using full-potential linear muffin-tin orbital (FP-LMTO) method is experimentally verified. The experimental tool used for the determination of the thermal and optical properties is the well-known photoacoustic technique. The variation of thermal diffusivity with changing x values in $Li_xMn_2O_4$ is extensively studied to explain the influence of lithium concentration on the thermal properties, and has been correlated with the structural asymmetry and defects in $Li_xMn_2O_4$. The optical absorption spectrum, being the signature of the electronic structure of materials, is recorded in the visible range (350–800 nm). Six prominent absorption peaks associated with the O $2p$-Mn t_{2g}, O $2p$-Mn e_g, and Mn t_{2g}-Mn e_g band transitions for $Li_xMn_2O_4$, with $x \leqslant 1$, are observed experimentally, substantiating the electronic structure predicted by the FP-LMTO method. However, it is observed that there are more absorption peaks in the case of $Li_{1.1}Mn_2O_4$ and $Li_{1.2}Mn_2O_4$, which is attributed to the structural distortion from pure cubic spinel structure to a mixture of spinel and tetragonal structures, which is verified by the x-ray diffraction spectra.

DOI: 10.1103/PhysRevB.76.115112 PACS number(s): 82.47.Aa, 71.20.−b, 78.20.Nv, 63.20.Mt

I. INTRODUCTION

Developments in the past few decades has made rechargeable lithium ion battery a major power source for about 60% of the portable devices used by today's mobile, information rich society. In Li-ion batteries, carbon electrode is used as the anode and lithium metal oxide (LMO) is the cathode, which acts as a rechargeable Li-ion source. The large structural stability with respect to changing Li content and the topotactic Li-intercalation mechanism of these lithium oxides form the basis of their application as cathodes in a rechargeable Li-ion battery.[1] The conventionally used LMO cathode is $LiCoO_2$, which acts as the source of Li ions that carry the electric charge through the electrolyte.[2] However, $LiMn_2O_4$ is widely recognized as a potential substitute for $LiCoO_2$, primarily because of its low cost and "green" (eco-friendly) nature. Moreover, unlike layered cobalt oxide materials, all atoms in spinel manganese oxides are connected via genuine chemical bonds with large channels in the lattice for Li insertion, and hence, they have low discharge capacity and structural stability at moderately high temperature.[3]

$LiMn_2O_4$ has cubic spinel structure (space group $Fd\bar{3}m$), with Li in tetrahedral sites and Mn in octahedral sites, as the stable phase at room temperature, although tetragonal and orthorhombic deformations are possible at low temperatures, which is the basic crystal structure at room temperature for materials having the general chemical composition AB_2O_4.[4,5] Nevertheless, $Li_2Mn_2O_4$, which corresponds to $x=2$ in $Li_xMn_2O_4$, has a tetragonal structure (space group $I4_1/amd$), whereas $LiMnO_2$ has an orthorhombic structure (space group $Pmmn$) and λ-MnO_2 has a layered structure (space group $R3m$), which are the commonly occurring cases. In addition, it has been reported that cubic spinel $LiMn_2O_4$ and orthorhombic $LiMnO_2$ structures show antiferromagnetism.[5]

The knowledge of thermal properties is of paramount importance since the limited Li cycling and storage performances of $LiMn_2O_4$ at elevated temperatures is a key issue in its commercial use.[6–8] Moreover, one of the major issues confronting the development of Li-ion batteries for electric vehicles and hybrid electric vehicles is the risk of thermal runaway under abusive conditions due to the large rise in temperature at the electrodes or in the electrolyte.[1] Besides, knowledge of the thermal properties such as thermal diffusivity and thermal conductivity can throw light on the structural properties of $Li_xMn_2O_4$ materials. The physical significance of the thermal diffusivity value as a measure of the speed of propagation of heat in the medium and of the inverse of thermal diffusivity as a measure of time required to establish the thermal equilibrium in a sample in which a transient temperature change has occurred is of vital importance in the context of devices under actual operating conditions when subjected to a thermal load. Basically, photoacoustic (PA) technique is a subset of photothermal (PT) techniques which work on the principle of light induced heating of a sample and the subsequent heat transmission in that material. The basic principle involving PA technique is the detection of pressure fluctuation resulting from heating of the sample surface and the surrounding medium following absorption of intensity modulated light beam by the sample. Hence, the PA signal (PT signal, in general) not only carries information regarding the absorbed light energy, which is the basis of their application in absorption spectroscopy, but also contains details regarding the thermal properties of the sample.[9–16]

Even though a large amount of research material has been published on the structural, electronic, and magnetic properties of $Li_xMn_2O_4$,[4,5,17–24] reports on the optical properties of $Li_xMn_2O_4$ are only few.[25,26] The reason for the scarcity of

studies about the optical properties may be due to the fact that the $Li_xMn_2O_4$ powders are optically opaque and most of the optical absorption spectroscopy studies rely on the transmission technique. Hence, we have employed photoacoustic spectroscopy (PAS) in determining the optical absorption spectrum of $Li_xMn_2O_4$ due to its unique advantage of directly measuring the amount of light absorbed by a material[27–32] and its zero-base-line advantage, which means signals are generated only if there is an optical absorption event. Moreover, scattered light, which presents such a serious problem in conventional spectroscopic techniques, presents less difficulty in PAS and can be solved by making necessary corrections.[33,34] The $Li_xMn_2O_4$ pelletized polycrystalline samples under the present investigation are highly absorbing, and hence, optically opaque in the range of experiment. This means that the PA signal produced is solely due to surface light absorption, and light scattering has negligible effect on the signal.

In the present work, the PA signal amplitude and phase from the samples measured in the reflection configuration[11,12,32] are simultaneously fitted using chi-square minimization procedure employing Rosencwaig-Gersho theory[32] for the determination of thermal diffusivity of $Li_xMn_2O_4$. The temperature rise in the sample surface is obtained by solving the three-dimensional (3D) heat diffusion equation for the calculation of pressure fluctuation inside the photoacoustic cell. The absorption spectra of the samples are recorded in the wavelength range of 350–800 nm using the photoacoustic technique. The observed effect of lithium concentration on the thermal diffusivity values of $Li_xMn_2O_4$ is correlated with the crystal structure modifications of $Li_xMn_2O_4$ obtained using x-ray diffraction (XRD) analysis. The various peaks in the PA optical absorption spectra are assigned and confirm experimentally the electronic structure predicted by the full-potential linear muffin-tin orbital (FP-LMTO) model.[18]

II. THEORY

The photothermal signal is generated when a periodically modulated light beam is absorbed by a sample, which is subsequently converted into heat. A part of this heat generated reaches the surface of the sample, where it heats a thin layer of the surrounding gas causing it to periodically expand and contract. This periodic modulation of the gas surrounding the sample whose thermal properties are to be determined causes pressure modulation inside the air-tight photoacoustic cell, which when detected by a sensitive microphone gives rise to the PA signal. According to the Rosencwaig-Gersho (RG) theory, this pressure variation inside the cell is given by[32]

$$\delta P(r,t) = \frac{\gamma P_0 \mu_g T(r,t)}{\sqrt{2} l_g T_0} e^{-i(\omega t - \pi/4)}, \tag{1}$$

where γ is the adiabatic gas constant, P_0 and T_0 the static pressure and temperature respectively, μ_g the thermal diffusion length of the gas, l_g the length of the gas volume inside the cell, and $T(r,t)$ the complex amplitude of temperature at

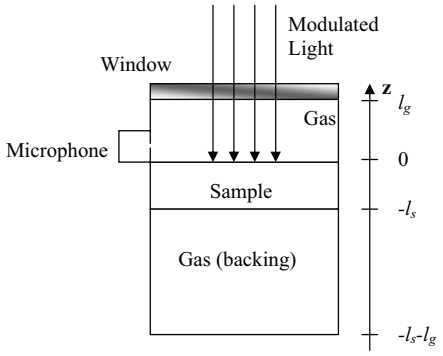

FIG. 1. Schematic of the experimental configuration.

the sample-gas boundary which can be determined by solving the heat diffusion equation in the three regions of interest, viz., gas, sample, and gas. The heat diffusion equation can be written as

$$\frac{\partial^2 T_i(r,t)}{\partial r^2} + \frac{1}{r}\frac{\partial T_i}{\partial r} + \frac{\partial^2 T_i}{\partial z^2} + \frac{Q}{k_i} = \frac{1}{\alpha_i}\frac{\partial T_i(r,t)}{\partial t}, \tag{2a}$$

where Q is the heat source term, k_i $(i=s,g)$ the thermal conductivity of sample and gas, and α_i $(i=s,g)$ the thermal diffusivity of sample and gas. Now we have to solve the heat diffusion equations for each layer by applying boundary conditions. In the present experiments, we have to consider three layers as shown in Fig. 1, i.e., front medium g (air), sample s, and backing g (air), and solve the heat diffusion equations for each layer, which is given below:

$$\frac{\partial^2 T_g}{\partial r^2} + \frac{1}{r}\frac{\partial T_g}{\partial r} + \frac{\partial^2 T_g}{\partial z^2} = \frac{1}{\alpha_g}\frac{\partial T_g}{\partial t}, \quad 0 \le z \le l_g \tag{2b}$$

for the gas in front of the sample.

$$\frac{\partial^2 T_s}{\partial r^2} + \frac{1}{r}\frac{\partial T_s}{\partial r} + \frac{\partial^2 T_s}{\partial z^2} = \frac{1}{\alpha_s}\frac{\partial T_s}{\partial t} - \frac{Q}{k_s}, \quad -l_s \le z \le 0, \tag{2c}$$

where the second term on the right hand side represents the source term as the sample absorbs light and acts as the source of heat, with $Q=(I_0\eta/2)\beta\exp(-\beta x)[1+\exp(j\omega t)]$. η is the light to heat conversion efficiency, I_0 the intensity, β the absorption coefficient at the excitation wavelength, and $\omega=2\pi f$, where f is the modulation frequency.

$$\frac{\partial^2 T_g}{\partial r^2} + \frac{1}{r}\frac{\partial T_g}{\partial r} + \frac{\partial^2 T_g}{\partial z^2} = \frac{1}{\alpha_g}\frac{\partial T_g}{\partial t}, \quad -l_s - l_g \le z \le -l_s \tag{2d}$$

for the backing (air). The boundary conditions are

$$T_g(z=0,t) = T_s(z=0,t), \quad k_s\frac{\partial T_s(z=0,t)}{\partial z} = k_g\frac{\partial T_g(z=0,t)}{\partial z},$$

$$T_g(z=-l,t) = T_s(z=-l,t),$$

$$k_s\frac{\partial T_s(z=-l,t)}{\partial z} = k_g\frac{\partial T_g(z=-l,t)}{\partial z},$$

$$T_g(z=\infty,t) = T_g(z=-\infty,t) = 0.$$

If the heating beam is Gaussian of power P and $1/e^2$ radius is a, then the source term Q can be written

$$Q(r,z,t) = \frac{\beta P \eta}{\pi a^2} \exp\left(-\frac{2r^2}{a^2}\right)\exp(\beta z)[1+\exp(j\omega t)]. \quad (3)$$

The above differential equations are reduced to a simpler partial differential equation by Hankel transformation $T_0(\lambda) = \int_0^\infty T(r) J_0(\lambda r) r dr$, where J_0 is the zeroth order Bessel function, i.e., $T(r,z,t) \rightarrow T_0(\lambda,z,t)$, and then by Laplace transformation, i.e., $T_0(\lambda,z,t) \rightarrow \Im_0(\lambda,z,p)$, these simpler partial differential equations are converted to ordinary differential equations which are easily solvable. Subsequently, Hankel inversion is applied and a steady state solution of the temperature distribution is derived for the three regions.[35–37] These temperature distribution equations, so obtained, have no analytical solution and, hence, have to be numerically solved. The three-dimensional heat diffusion equations corresponding to the gas-sample-gas system, in order to calculate the temperature distribution at the sample surface, are numerically solved using MATLAB. The temperature distribution, thus obtained, is used to calculate the pressure variation in the cell using Eq. (1), from which the amplitude and phase of the photoacoustic signal can be obtained. The thermal diffusivity values are determined using chi-square minimization procedure by fitting the experimental amplitude and phase with the theoretical plots generated.

III. EXPERIMENT

Although a large number of routes are available for the preparation of $Li_xMn_2O_4$, powders in the present work are prepared by a well-known direct solid-state reaction of Li_2CO_3 and $MnCO_3$,[8,25] and these powders are made into pellets by applying a constant load of 7 tons. The concentration of Li in $Li_xMn_2O_4$ samples is varied by changing the molar ratio of Li_2CO_3 to $MnCO_3$.

The thermal diffusivity values and optical absorption spectra of $Li_xMn_2O_4$ are obtained using PA technique with a homemade PA cell employed in reflection configuration. To determine the thermal diffusivity values of $Li_xMn_2O_4$ pellets, light beam from a 20 mW He-Ne laser (632.8 nm) is modulated using a mechanical chopper (SR 540) which is allowed to fall on a sample that is fixed to the PA cell. The modulation frequency is varied from 5 to 400 Hz, and the corresponding modulated pressure signal generated is detected by a commercial condenser microphone. The output signal from the microphone is fed to a lock-in amplifier (SR 830) through a preamplifier (SR 550). All the instruments are computer controlled using the RS-232 port of a personal computer. The experimental setup is standardized using a commercially available Si wafer whose thermal diffusivity is calculated to be 0.81×10^{-4} m^2 s^{-1}, which is in perfect agreement with the standard values.

For the absorption spectra measurements, the experimental setup is the same as for the thermal diffusivity measurements, with the He-Ne laser being replaced by a 250 W quartz tungsten halogen lamp. A monochromator attached to the output side of the tungsten halogen lamp selects the wavelength of excitation at a resolution of 5 nm. The excitation beam is modulated at a constant frequency of 10 Hz.

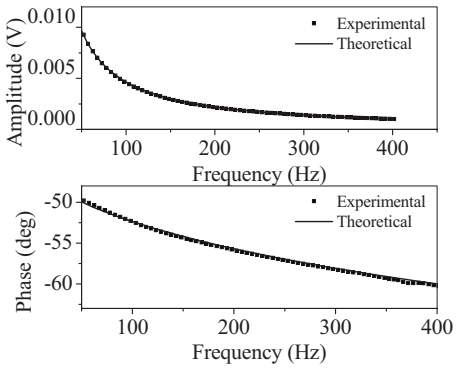

FIG. 2. The experimentally obtained and theoretically fitted amplitude and phase variation of $LiMn_2O_4$ with frequency.

IV. RESULTS AND DISCUSSION

A. Variation of thermal diffusivity values of $Li_xMn_2O_4$ with x

For the sake of saving space and avoiding redundancy, in this paper we include only one experimental curve showing the variation of PA signal amplitude and phase with frequency, corresponding to $LiMn_2O_4$. Figure 2 shows the variation of amplitude and phase for $LiMn_2O_4$ with frequency and the fitted theoretical curve obtained using chi-square minimization for determining thermal diffusivity. The frequency range used in fitting is only from 50 to 400 Hz in order to avoid any bad response of microphone in the low frequency region. In determining the temperature distribution at the sample surface which is used to calculate the pressure variation inside the PA cell, the complex 3D heat diffusion equations are solved instead of the much simpler one-dimensional 1D case. This is done taking into account the spot size (~4 mm) used in the experiment and thereby avoiding any error that can arise from the 3D effects while fitting the amplitude and phase in determining the thermal diffusivity.[38] The 3D effect on the PA signal for various spot sizes is shown in Fig. 3 for the case of $LiMn_2O_4$. Though in the amplitude plot there is no clear difference between 1D and 3D theory, in the phase plot the difference is evident. It is observed that for larger spot sizes, the 3D curves converge toward the one-dimensional case. Since we are simultaneously fitting both amplitude and phase plots to obtain thermal diffusivity, in order to minimize the error in thermal diffusivity values while fitting the data due to limited spot size, we used the 3D thermal diffusion equations. The thermal diffusivity values of $Li_xMn_2O_4$ for various values of x are tabulated in Table I and their variation is shown graphically in Fig. 4 for better understanding. It can be seen that thermal diffusivity of $LiMn_2O_4$, i.e., $x=1$, is the highest among the group of $Li_xMn_2O_4$ samples considered under the present study, with the diffusivity value monotonically decreasing with an increase or decrease in x values.

The heat generation and transport mechanisms in $Li_xMn_2O_4$ can be explained on the basis of those in semiconductors due to the fact that $LiMn_2O_4$ is a small-polaron semi-

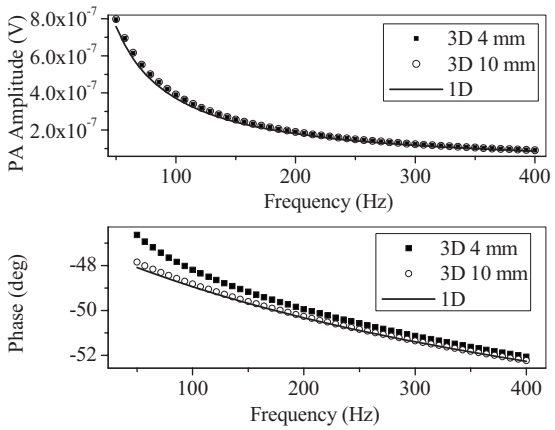

FIG. 3. The variation of PA amplitude and phase with respect to frequency for $LiMn_2O_4$, plotted using 3D heat diffusion equation for different beam diameters (4 and 10 mm) and using 1D heat diffusion equation.

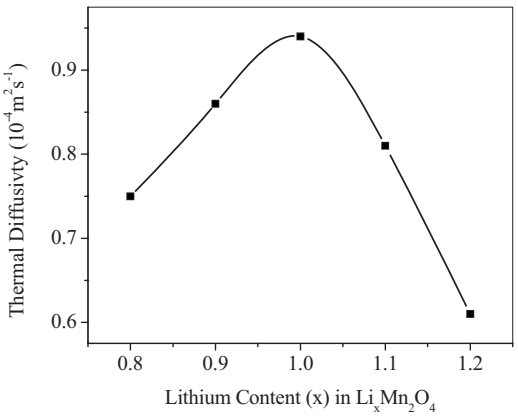

FIG. 4. Variation of thermal diffusivity with respect to Li content in $Li_xMn_2O_4$.

conductor since the e_g electrons on Mn^{3+} ions are trapped in local lattice relaxations and, as a result, their mobility carries an activation energy.[39] The heat generation due to absorption in semiconductors when irradiated with an intensity modulated light beam arises due to three processes, namely, thermalization (time scale of the order of picoseconds) due to intraband transitions of photogenerated carriers, and nonradiative bulk recombination and surface recombination due to interband transitions of photogenerated carriers. All these different mechanisms finally result in the creation of heat energy, which is then transferred to the lattice through the creation of phonons. At low modulation frequencies of photothermal experiments, the contribution to the heat flow by the bulk and surface recombination mechanisms is negligibly small and, hence, the photoacoustic signal, obtained in this experiment, which employs low modulation frequencies, is solely due to the thermal wave component of the phonon-assisted heat conduction process.[40] This phonon-assisted heat conduction is adversely affected by phonon-phonon interactions and phonon scattering by imperfections and at boundaries. Moreover, recent studies on $LiMn_2O_4$ have shown that the phonons due to the vibrational modes of $LiMn_2O_4$ are due to the complex movements involving all the atoms of the crystal structure rather than due to individual LiO_4 tetrahedron vibrational modes and MnO_6 octahedron vibrational modes.[24]

From the fact that the thermal diffusivity value of $LiMn_2O_4$ is the maximum among $Li_xMn_2O_4$ samples, it can be inferred that the crystal structure is less distorted at $x=1$ for $Li_xMn_2O_4$ because the thermal diffusivity value can be treated as a direct measure of phonon group velocity and phonon scattering. That is, the higher the phonon scattering, the lower will be the phonon group velocity and, hence, the lesser will be the thermal conductivity and diffusivity values.[8] The delithiated form of $Li_xMn_2O_4$, λ-MnO_2, is considered to be an ionic crystal having Mn^{4+} in tetravalent state. On the other hand, it has been observed that Li^+ in $LiMn_2O_4$ is fully ionized, which demands a reduction in the valency of Mn from 4 to 3.5, which is believed to be achieved by reducing 50% of Mn^{4+} ions in λ-MnO_2 to Mn^{3+} ions. In fact, $LiMn_2O_4$ can be considered as $LiMn^{3+}Mn^{4+}O_4$ with an equal number of isotropic $Mn^{4+}O_4$ octahedra and Jahn-Teller-distorted $Mn^{3+}O_4$ octahedra.[20] In $Li_xMn_2O_4$, for $x \leqslant 1$, Li cations are on 8*a* tetrahedral sites, Mn cations on 16*d* octahedral sites, and O anions on 32*e* positions, which give rise to a cubic spinel structure. In fact, $Li_xMn_2O_4$ can be represented by a supercell as $[(Li_8)^{8a}(Mn_{16})^{16d}(O_{32})^{32e}]$ with clear representation of the number and position of each type of atom in it.[41] An important feature of the spinel structure is that each 8*a* tetrahedron shares all four faces with 16*c* octahedra. The maximum tetrahedral-site occupancy is 50% as in $LiMn_2O_4$, which corresponds to $x=1$ and brings more structural symmetry to this structure compared to $Li_xMn_2O_4$, with $x<1$. However, when $x>1$, in addition to the 8*a* tetrahedral sites, the vacant 16*c* octahedral sites also get occupied with Li ions,[6] which can be represented in the supercell model as $[(Li_8)^{8a}(Li_y)^{16c}(Mn_{16})^{16d}(O_{32})^{32e}]$, with y taking values from 1 to 8. This is consistent with our observation that the deviation in the XRD pattern from the cubic spinel structure starts around $x=1$, as shown in Fig. 5. It is quite evident in the XRD pattern that for $x=1.1$ and 1.2 in $Li_xMn_2O_4$, additional peaks at 16.8° and 34.5°, other than that of cubic spinel structure, appear. It is supposed that these extra peaks correspond to the Li occupancy of the octahedral, interstitial 16*c* sites in addition to the 8*a* octahedral sites, suggesting that the crystal structure is in a slightly mixed phase. The filling up of vacant 16*c* sites by Li ions along with the complete transfer

TABLE I. Thermal diffusivity values of $Li_xMn_2O_4$, with $x=0.8$, 0.9, 1.0, 1.1, and 1.2.

	$Li_{0.8}Mn_2O_4$	$Li_{0.9}Mn_2O_4$	$LiMn_2O_4$	$Li_{1.1}Mn_2O_4$	$Li_{1.2}Mn_2O_4$
Thermal diffusivity (10^{-4} m^2/s)	0.75±0.01	0.86±0.012	0.94±0.015	0.81±0.012	0.61±0.01

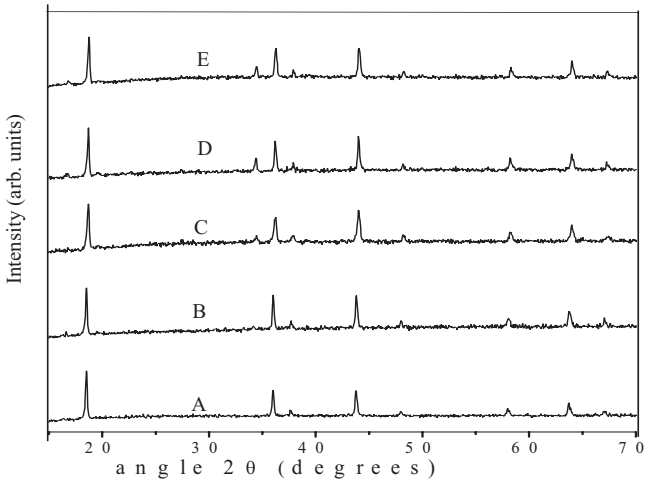

FIG. 5. XRD spectra of $Li_xMn_2O_4$ with $x=0.8$ (A), 0.9 (B), 1.0 (C), 1.1 (D), and 1.2 (E).

of Li ions from 8*a* sites to 16*c* sites results in the tetragonal structure of $Li_2Mn_2O_4$. Therefore, when $x<1$ in $Li_xMn_2O_4$, less than 50% of the available 8*a* sites are filled by Li ions and when $x>1$, in addition to the 8*a* sites, 16*c* interstitial sites are also occupied with Li ions; both effects cause a reduction in symmetry and are sources of defects. The phonon scattering and a subsequent decrease of phonon group velocity decreases with crystal symmetry and increases with defects. Thus, it can be argued that the crystal structure of $Li_xMn_2O_4$ with maximum symmetry and minimum defects is that with $x=1$, which corresponds to $LiMn_2O_4$. Therefore, it is quite evident why the thermal diffusivity of $LiMn_2O_4$ is greater than other samples in the range of Li content studied in this work.

It should to be noted that the value of thermal diffusivity obtained for $LiMn_2O_4$ in the present study is consistent with a previous study comparing the thermal diffusivities of $LiMn_2O_4$ and λ-MnO_2, which are respectively 0.93×10^{-4} and 0.11×10^{-4} m^2 s^{-1}.[8] The cause of reduction of thermal diffusivity upon Li deintercalation of $LiMn_2O_4$ is attributed to the increase in phonon scattering due to reduction in crystal symmetry, which is consistent with our previous study.[8] Comparing the results of the present study and our previous study, it can be deduced that the thermal diffusivity of $LiMn_2O_4$ is the maximum among $Li_xMn_2O_4$ $(0<x<1.2)$ and decreases steadily as the Li concentration decreases, reaching a minimum for λ-MnO_2. The variation in thermal diffusivity values with Li content is significant due to the fact that during the actual operation of a Li-ion battery, thermal diffusivity of the $Li_xMn_2O_4$ cathode will be increasing with respect to its Li content. In other words, thermal diffusivity of Li battery cathode (λ-MnO_2) will be increasing during Li intercalation, which happens during Li-ion battery discharging. Similarly, thermal diffusivity of Li-ion battery cathode ($LiMn_2O_4$) decreases during Li-ion battery charging as Li is deintercalated from it.

B. Spectroscopic studies on $Li_xMn_2O_4$

The PA spectra of $Li_xMn_2O_4$ samples are shown in Fig. 6.

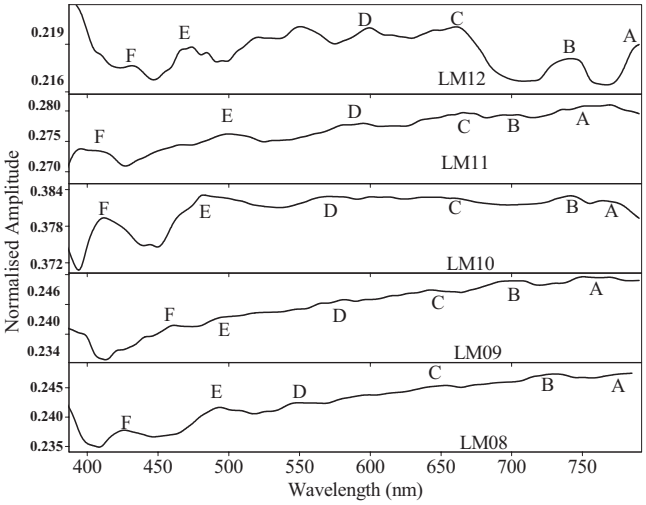

FIG. 6. Absorption spectra of $Li_xMn_2O_4$ with $x=0.8$ (LM08), 0.9 (LM09), 1.0 (LM10), 1.1 (LM11), and 1.2 (LM12). The various absorption peaks are marked A, B, C, D, E, and F, whose energy values are given in Table III.

It may be noted that the PA spectra are given in terms of wavelength in order to facilitate good visibility of the absorption peaks and also since the signal is recorded in linear steps of wavelength. The resolution of the measurements is restricted to 5 nm (0.02 eV at 575 nm) to have a good signal to noise ratio. The appearance of peaks in the absorption spectrum and their shift, if any, with respect to Li content of $Li_xMn_2O_4$ can be ascribed to the influence of cell volume and cell structure on the electronic structure and band formation. This is due to the fact that the electron density of states of $Li_xMn_2O_4$ is related to the volume of the unit cell of the crystal. Though in most of the studies it has been observed that the cell volume of $Li_xMn_2O_4$ is proportional to x,[42,43] it has been theoretically predicted that the cell volume change of $Li_xMn_2O_4$ on Li intercalation can be either positive or negative depending on the value of x in $Li_xMn_2O_4$.[12] When Li is added to $Li_xMn_2O_4$, one of the tendencies of the lattice is to expand because of the decrease in Mn valency from 4 to

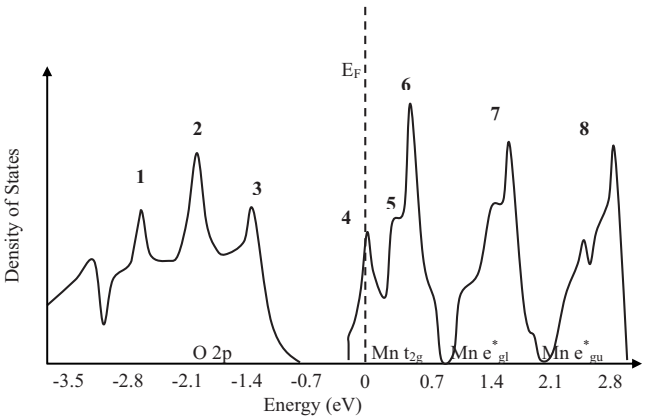

FIG. 7. Schematic diagram of the electron density of states of $LiMn_2O_4$ as given by Grechnev *et al.* (Ref. 7). The relevant band peaks of O 2*p*, Mn t_{2g}, Mn e^*_{gl}, and Mn e^*_{gu} are marked and their corresponding energies are given in Table II.

TABLE II. Energies corresponding to the various peaks in the electron density of states of $Li_xMn_2O_4$, according to Grechnev *et al.* (Ref. 18).

Band	1	2	3	4	5	6	7	8
Peak	O $2p_1$	O $2p_m$	O $2p_u$	Mn t_{2gl}	Mn t_{2gm}	Mn t_{2gu}	Mn e^*_{gl}	Mn e^*_{gu}
Energy (eV)	−2.8	−1.8	−1.4	0	0.45	0.6	1.4–1.6	2.7

3, causing a lowering of the Mn—O bond order. However, the Coulomb attractive interaction between Li^+ and O anion can lead to a decrease in the cell volume, especially at higher Li content. These two opposing tendencies determine the cell volume change upon Li intercalation.

Before going into the detailed analysis of the absorption spectra and identification of the peaks, the various bands present in $Li_xMn_2O_4$ are outlined. Since the Mn ion is in octahedral symmetry, the electronic structure of $Li_xMn_2O_4$ compounds is governed by a strong hybridization between the Mn d and O p atomic orbitals, where its d_{z^2} and $d_{x^2-y^2}$ atomic orbitals directly overlap with the p_x, p_y, and p_z orbitals of oxygen along the octahedral directions. This σ overlap creates the e_g bands, of which the bonding band, e^b_g, has a predominant oxygen p character and the antibonding band e^*_g, has a predominant metallic d character. The remaining d_{xy}, d_{yz}, and d_{xz} orbitals point away from oxygen and have only a slight π overlap, giving rise to the nonbonding t_{2g} bands. In $Li_xMn_2O_4$ spinels, the Fermi level E_F lies within the partially filled nonbonding t_{2g} bands.[4,18,20,40] Similarly, the overlap of O p with Mn p and O p with Mn s gives rise to t_{1u} and a_{1g} bands, respectively. However, there is considerable amount of intermixing between e^b_g, t_{1u}, and a_{1g} bands and are collectively known as O $2p$ bands because of their predominant O p character.[20,25]

In order to fully explain all the absorption peaks of $Li_xMn_2O_4$, a schematic view of the electronic density of states of the corresponding spinel structure presented by Grechnev *et al.* using the FP-LMTO method is shown in Fig. 7.[18] The band energy corresponding to 0 eV represents the fermi level which resides in Mn t_{2g} band. The bands lying above Mn t_{2g} band are the lower Mn e^*_g, Mn e^*_{gl} bands and the upper Mn e^*_g, Mn e^*_{gu} bands. It is noteworthy that the density of states of O $2p$ and Mn t_{2g} bands has a few sharp peaks, and their identification with the corresponding energy values are given in Table II. The Arabic numerals in this table are used to facilitate the identification of their position in the electron density of states.

Table III gives the observed peak values of the absorption spectra of $Li_xMn_2O_4$ samples and the association of their origin with the corresponding electronic transitions between the various peaks of electron density of states, given in Table II, indicating their energy differences. It may be noted that many transitions between the band peaks have coinciding energy, thus reducing the number of observable absorption peaks. Further, it is evident that there are no absorption peaks appearing in the photon energy range of 2.2–2.5 eV in the case of $Li_xMn_2O_4$, with $x \leqslant 1$, where the crystal structure is assumed to be purely spinel. It is remarkable that all the observed absorption peaks have a one to one correspondence with the theoretically presented electron density of states by the FP-LMTO method by Grechnev *et al.*[18] However, it can be seen that there are small differences between the experimentally observed absorption peaks and the theoretically predicted ones, which may be due to the band structure differences of $Li_xMn_2O_4$ from $LiMn_2O_4$ and may also be due to deviations from the exact compositional stoichiometry of the samples. Moreover, the overall behavior of the absorption

TABLE III. Experimentally determined energies of absorption peaks of $Li_xMn_2O_4$ and the corresponding band transitions with energy values.

	$Li_{0.8}Mn_2O_4$	$Li_{0.9}Mn_2O_4$	$LiMn_2O_4$	$Li_{1.1}Mn_2O_4$	$Li_{1.2}Mn_2O_4$
(A) Mn t_{2gl}-Mn e^*_{gl} (1.4–1.6 eV)	790 nm (1.57 eV)	750 nm (1.62 eV)	770 nm (1.61 eV)	775 nm (1.60 eV)	790 nm (1.57 eV)
(B) O $2p_m$-Mn t_{2gl} (1.8 eV)	720 nm (1.72 eV)	700 nm (1.78 eV)	740 nm (1.68 eV)	740 nm (1.68 eV)	745 nm (1.66 eV)
(C) O $2p_u$-Mn t_{2gu} (2.0 eV)	645 nm (1.92 eV)	640 nm (1.94 eV)	660 nm (1.88 eV)	670 nm (1.85 eV)	665 nm (1.87 eV)
(D) O $2p_l$-Mn t_{2gl} (2.2 eV)	545 nm (2.28 eV)	575 nm (2.17 eV)	575 nm (2.17 eV)	585 nm (2.12 eV)	590 nm (2.10 eV)
(E) O $2p_l$-Mn t_{2gm} (2.6 eV)	495 nm (2.50 eV)	480 nm (2.58 eV)	485 nm (2.55 eV)	495 nm (2.50 eV)	475 nm (2.60 eV)
(F) Mn t_{2gl}-Mn e^*_{gu} (2.7 eV), O $2p_l$-Mn t_{2gu} (2.8 eV), and O $2p_u$-Mn e^*_{gl} (2.8–3 eV)	435 nm (2.85 eV)	454 nm (2.73 eV)	410 nm (3.02 eV)	430 nm (2.88 eV)	440 nm (2.82 eV)

spectrum of pelletized $LiMn_2O_4$ powder in the present study is similar to the spectrum calculated by Grechnev *et al.* except for the manifestation of a few peaks in our spectrum.[18] However, if closely observed, one can see that there are some undulations in that theoretical curve of Ref. 18. Moreover, the absorption curve obtained by Kushida and Kuriyame in Ref. 26 for $LiMn_2O_4$ thin film using transmission spectroscopy is also similar to the present spectrum, and the small difference in the two spectra may be due to the difference in the physical nature of the samples, thin film in Ref. 26 and pelletized powder in the present case.

There is only a negligible shift in the position of the peaks as x varies, though there are a few peaks appearing in the energy range of 2.2–2.5 eV for $Li_xMn_2O_4$, with $x>1$. Some of those additional peaks are the peaks at 520 nm (2.38 eV) and at 550 nm (2.25 eV) and the cluster of peaks between 470 and 490 nm, occurring in the case of $Li_{1.2}Mn_2O_4$. We propose the following explanation for not observing any considerable shift in the peak as well as for the additional peaks occurring for $x>1$. As mentioned before, the shift in peaks is controlled by the cell volume changes as the x value changes. However, in the present study where x changes from 0.8 to 1.2, the cell volume is found to be almost a constant, which is quite obvious from the XRD data of $Li_xMn_2O_4$ as the position of their diffraction peaks does not change with x. In fact, the cubic lattice constant for $LiMn_2O_4$ is determined as 8.242 Å and its cell volume is 5.599×10^{-28} m^3. The additional peaks appearing for $Li_{1.1}Mn_2O_4$ and $Li_{1.2}Mn_2O_4$ can be ascribed to the appearance of a tetragonal structure, as a structural distortion, in the cubic structure. Moreover, in the case of $Li_{1.1}Mn_2O_4$, unlike that of $Li_{1.2}Mn_2O_4$, these additional peaks are not easily observable except for a few small humps on the spectra, because the structural distortion due to the tetragonal structure is relatively small in $Li_{1.1}Mn_2O_4$. It may also be noted that the electron density of states corresponding to the tetragonal state has more peaks than the corresponding spinel state.[5] Since the Mn=O bond length remains almost a constant for the various $Li_xMn_2O_4$ samples, the only possibility for deviation in the absorption spectra for higher Li content is the change in the shape of the crystal structure from pure cubic spinel shape for low Li content samples to a mixture of cubic spinel and tetragonal phases in the case of higher Li content $Li_xMn_2O_4$ samples, which fully validates our observation from the XRD data that the crystal phase is not pure spinel but a mixture of cubic and tetragonal structures.

V. CONCLUSIONS

From the PA measurements and the subsequent theoretical analysis using 3D heat diffusion equation and RG theory, thermal diffusivity values of $Li_xMn_2O_4$ are determined. It is observed that the diffusivity value of $LiMn_2O_4$ is significantly higher than the rest of the group and that thermal diffusivity value decreases monotonically as the Li content changes from $x=1$, which is the case for $LiMn_2O_4$. Therefore, thermal diffusivity value of $LiMn_2O_4$ cathode and, hence, its heat dissipation capability is not a constant in time during the operation of $LiMn_2O_4$-based Li-ion battery, but increases in accordance with the Li content. This observation of the variation of thermal diffusivity with Li content can shed light on the heat propagation mechanisms in the $LiMn_2O_4$ cathodes and may lead to addressing the thermal stability issues related to $LiMn_2O_4$-based Li-ion batteries. It is proposed that one of the contributing factors in the decrease of thermal diffusivity values of $Li_xMn_2O_4$ from that of $LiMn_2O_4$ is the symmetry of the crystal structure, which is the maximum for $LiMn_2O_4$. Moreover, the vacant 8*a* tetrahedral sites in the case of $Li_xMn_2O_4$ with $x<1$ and the occupied 16*c* interstitial sites in the case of $x>1$ are found to be the other major sources of crystal defects resulting in a reduction in thermal diffusivity values of $Li_xMn_2O_4$ with $x<1$ and $x>1$ compared with $x=1$.

The spectroscopic measurements on $Li_xMn_2O_4$ revealed several peaks in their absorption spectra which are associated with the electron density of states determined by the FP-LMTO method by Grechnev *et al.*,[18] providing a strong experimental verification of these calculations. On the basis of the number of absorption peaks in each spectrum, it is possible to classify $Li_xMn_2O_4$ into two groups with respect to x, i.e., its Li content, as group with $x\leqslant1$ and group with $x>1$. The reason for the separation of $Li_xMn_2O_4$ into two groups is assumed to be the appearance of a tetragonal phase in addition to the cubic spinel phase in $Li_xMn_2O_4$ when $x>1$. This assumption is further justified by the appearance of additional diffraction peaks in the case of $Li_xMn_2O_4$ when $x>1$.

ACKNOWLEDGMENTS

One of the authors (T.L.S.) wishes to thank Vinu V. Namboory, Rajesh Pillai, Manesh Gopinath, Jijo P. Ulahannan, Iswarya Mathew, Lekshmi Sasidhar, and A. Santhi for their efforts in collecting articles needed for this work. He is also grateful to Nibu A. George, K. C. Sebastian, and B. Ravindranathan Nair for their constant encouragement. Two of the authors (R.T. and S.J.) acknowledge the financial support by KSCSTE, and another author (K.R.) expresses his gratitude for the financial aid by UGC. This work was supported partially by Grants Nos. Milenio ICM P02-049F, MECESUP USA0108, and MECESUP UCO0209 and Project No. 207.011.047-1.0 from Direccion de Investigacion, Universidad de Concepcion.

[1] H. Yang, S. Amiruddin, H. J. Bang, Y. K. Sun, and J. Prakash, J. Ind. Eng. Chem. (Seoul, Repub. Korea) **12**, 12 (2006).
[2] H. T. Huang and P. G. Bruce, J. Power Sources **54**, 52 (1995).
[3] J.-M. Tarascon and M. Armand, Nature (London) **414**, 359 (2001).
[4] H. Yamaguchi, A. Yamada, and H. Uwe, Phys. Rev. B **58**, 8 (1999).
[5] S. K. Mishra and G. Ceder, Phys. Rev. B **59**, 6120 (1999).
[6] M. M. Thackeray, M. F. Mansuetto, D. W. Dees, and D. R. Vissers, Mater. Res. Bull. **31**, 133 (1996).
[7] L. Pascual, M. L. Perez-Revenga, R. M. Rojas, J. M. Rojo, and J. M. Amarilla, Electrochim. Acta **51**, 3193 (2006).
[8] K. Raveendranath, J. Ravi, S. Jayalekshmi, T. M. A. Rasheed, and K. P. R. Nair, Mater. Sci. Eng., B **131**, 210 (2006).
[9] S. D. George, S. Saravanan, M. R. Anantharaman, S. Venkatachalam, P. Radhakrishnan, V. P. N. Nampoori, and C. P. G. Vallabhan, Phys. Rev. B **69**, 235201 (2004).
[10] J. Ravi, M. K. Jayaraj, K. A. Vanaja, K. P. R. Nair, and T. M. A. Rasheed, Semicond. Sci. Technol. **18**, 693 (2003).
[11] J. Thoen and C. Glorieux, Thermochim. Acta **305**, 137 (1997).
[12] C. Glorieux, J. Fivez, and J. Thoen, J. Appl. Phys. **73**, 684 (1993).
[13] A. K. Rai and J. P. Singh, Instrum. Sci. Technol. **31**, 323 (2003).
[14] Y. Fan, A. Mandelis, G. Spirou, I. A. Vitkin, and W. M. Whelan, Phys. Rev. E **72**, 051908 (2005).
[15] A. C. Bento, F. C. G. Gandra, E. C. Dasilva, H. Vargas, and L. C. M. Miranda, Phys. Rev. B **45**, 5031 (1992).
[16] K. N. Madhusoodanan, J. Philip, G. Parthasarathy, S. Asokan, and E. S. R. Gopal, Philos. Mag. B **58**, 123 (1988).
[17] W. I. F. David, M. M. Thackeray, L. A. De Picciotto, and J. B. Goodenough, J. Solid State Chem. **67**, 316 (1987).
[18] G. E. Grechnev, R. Ahuja, B. Johansson, and O. Eriksson, Phys. Rev. B **65**, 174408 (2002).
[19] J. Molenda, S. Swierczek, M. Molenda, and J. Marzec, Solid State Ionics **135**, 53 (2000).
[20] M. K. Aydinol, A. F. Kohan, G. Ceder, K. Cho, and J. Joannopoulos, Phys. Rev. B **56**, 1354 (1997).
[21] Y. Liu, T. Fujiwara, H. Yukawa, and M. Morinaga, Solid State Ionics **126**, 209 (1999).
[22] L. Ning, J. Wu, C. Zhou, S. Yao, Z. Pi, and H. Cheng, Int. J. Quantum Chem. **107**, 225 (2007).
[23] A. Paolone, P. Roy, G. Rousse, C. Masquelier, and J. Rodriguez-Carvajal, Solid State Commun. **111**, 453 (1999).
[24] A. Paolone, C. Castellano, R. Cantelli, G. Rousse, and C. Masquelier, Phys. Rev. B **68**, 014108 (2003).
[25] S. Thomas Lee, K. Raveendranath, K. Rajive Tomy, M. Paulraj, S. Jayalekshmi, and Jyotsna Ravi, Appl. Phys. Lett. **90**, 161912 (2007).
[26] K. Kushida and K. Kuriyama, Appl. Phys. Lett. **77**, 4154 (2000).
[27] A. Rosencwaig, Phys. Today **28**, 23 (1975).
[28] G. A. West, J. J. Barrett, D. R. Siebert, and K. V. Reddy, Rev. Sci. Instrum. **54**, 797 (1983).
[29] N. A. George, J. Ravi, S. T. Lee, B. Aneeshkumar, J. Thomas, V. P. N. Nampoori, and P. Radhakrishnan, Opt. Mater. (Amsterdam, Neth.) **27**, 1593 (2005).
[30] J. P. Lima, H. Vargas, A. Miklos, M. Angelmahr, and P. Hess, Appl. Phys. B: Lasers Opt. **85**, 279 (2006).
[31] M. Angelmahr, A. Miklos, and P. Hess, Appl. Phys. B: Lasers Opt. **85**, 285 (2006).
[32] A. Rosencwaig and A. Gersho, J. Appl. Phys. **47**, 64 (1976).
[33] P. Helander, N. Lundstrom, and D. McQueen, J. Appl. Phys. **51**, 3841 (1980).
[34] P. Helander, J. Appl. Phys. **54**, 3410 (1983).
[35] W. B. Jackson, N. M. Amer, A. C. Boccara, and D. Fournier, Appl. Opt. **20**, 1333 (1981).
[36] L. C. Aamodt and J. C. Murphy, J. Appl. Phys. **52**, 4903 (1981).
[37] *Photothermal Investigations of Solids and Fluids*, edited by Jeffrey A. Sell (Academic, New York, 1989), pp. 53–61.
[38] J. Ravi, Y. Lu, S. Longuemart, S. Paoloni, H. Pfeiffer, J. Thoen, and C. Glorieux, J. Appl. Phys. **97**, 014701 (2005).
[39] E. Iguchi, N. Nakamura, and A. Aoki, Philos. Mag. B **78**, 65 (1998).
[40] N. A. George, C. P. G. Vallabhan, V. P. N. Nampoori, and P. Radhakrishnan, Opt. Eng. (Bellingham) **41**, 251 (2002).
[41] T. Minami, M. Tatsumisago, M. Wakihara, C. Iwakura, S. Kohjiya, and I. Tanaka, *Solid State Ionics for Batteries* (Springer, Tokyo, 2005), pp. 258–269.
[42] H. Berg and J. O. Thomas, Solid State Ionics **126**, 227 (1999).
[43] M. M. Thackeray, W. I. F. David, P. G. Bruce, and J. B. Goodenough, Mater. Res. Bull. **18**, 461 (1983).